

Systematic Identification of LAEs for Visible Exploration and Reionization Research Using Subaru HSC (SILVERRUSH). I.

Program Strategy and Clustering Properties of $\sim 2,000$ $\text{Ly}\alpha$ Emitters at $z = 6 - 7$ over the $0.3 - 0.5 \text{ Gpc}^2$ Survey Area

Masami OUCHI,^{1,2} Yuichi HARIKANE,^{1,3} Takatoshi SHIBUYA,¹ Kazuhiro SHIMASAKU,^{4,5} Yoshiaki TANIGUCHI,⁶ Akira KONNO,^{1,4} Masakazu KOBAYASHI,⁷ Masaru KAJISAWA,⁸ Tohru NAGAO,⁸ Yoshiaki ONO,¹ Akio K. INOUE,⁹ Masayuki UMEMURA,¹⁰ Masao MORI,¹⁰ Kenji HASEGAWA,¹¹ Ryo HIGUCHI,¹ Yutaka KOMIYAMA,^{12,13} Yuichi MATSUDA,^{12,13} Kimihiko NAKAJIMA,¹⁴ Tomoki SAITO,¹⁵ and Shiang-Yu WANG,¹⁶

¹Institute for Cosmic Ray Research, The University of Tokyo, 5-1-5 Kashiwanoha, Kashiwa, Chiba 277-8582, Japan

²Kavli Institute for the Physics and Mathematics of the Universe (Kavli IPMU, WPI), The University of Tokyo, 5-1-5 Kashiwanoha, Kashiwa, Chiba, 277-8583, Japan

³Department of Physics, Graduate School of Science, The University of Tokyo, 7-3-1 Hongo, Bunkyo, Tokyo, 113-0033, Japan

⁴Department of Astronomy, Graduate School of Science, The University of Tokyo, 7-3-1 Hongo, Bunkyo, Tokyo 113-0033, Japan

⁵Research Center for the Early Universe, Graduate School of Science, The University of Tokyo, 7-3-1 Hongo, Bunkyo, Tokyo 113-0033, Japan

⁶The Open University of Japan, Wakaba 2-11, Mihama-ku, Chiba 261-8586, Japan

⁷Faculty of Natural Sciences, National Institute of Technology, Kure College, 2-2-11 Agaminami, Kure, Hiroshima 737-8506, Japan

⁸Research Center for Space and Cosmic Evolution, Ehime University, Bunkyo-cho, Matsuyama, Ehime 790-8577, Japan

⁹Department of Environmental Science and Technology, Faculty of Design Technology, Osaka Sangyo University, 3-1-1, Nagaito, Daito, Osaka 574-8530, Japan

¹⁰Center for Computational Sciences, University of Tsukuba, 1-1-1 Tennodai, Tsukuba 305-8577 Ibaraki, Japan

¹¹Department of Physics and Astrophysics, Nagoya University Furo-cho, Chikusa-ku, Nagoya, Aichi 464-8602, Japan

¹²National Astronomical Observatory of Japan, 2-21-1 Osawa, Mitaka, Tokyo 181-8588

¹³The Graduate University for Advanced Studies (SOKENDAI), 2-21-1 Osawa, Mitaka, Tokyo 181-8588

¹⁴European Southern Observatory, Karl-Schwarzschild-Str. 2, D-85748 Garching bei Munchen, Germany

¹⁵Nishi-Harima Astronomical Observatory, Center for Astronomy, University of Hyogo, 407-2 Nishigaichi, Sayo-cho, Sayo, Hyogo 679-5313, Japan

¹⁶Academia Sinica, Institute of Astronomy and Astrophysics 11F of AS/NTU

Astronomy-Mathematics Building, No.1, Sec. 4, Roosevelt Rd, Taipei 10617, Taiwan

[‡]Based on data obtained with the Subaru Telescope. The Subaru Telescope is operated by the National Astronomical Observatory of Japan.

*E-mail: ouchims@icrr.u-tokyo.ac.jp

Received ; Accepted

Abstract

We present the SILVERRUSH program strategy and clustering properties investigated with $\sim 2,000$ Ly α emitters at $z = 5.7$ and 6.6 found in the early data of the Hyper Suprime-Cam (HSC) Subaru Strategic Program survey exploiting the carefully designed narrowband filters. We derive angular correlation functions with the unprecedentedly large samples of LAEs at $z = 6 - 7$ over the large total area of $14 - 21$ deg² corresponding to $0.3 - 0.5$ comoving Gpc². We obtain the average large-scale bias values of $b_{\text{avg}} = 4.1 \pm 0.2$ (4.5 ± 0.6) at $z = 5.7$ ($z = 6.6$) for $\gtrsim L^*$ LAEs, indicating the weak evolution of LAE clustering from $z = 5.7$ to 6.6 . We compare the LAE clustering results with two independent theoretical models that suggest an increase of an LAE clustering signal by the patchy ionized bubbles at the epoch of reionization (EoR), and estimate the neutral hydrogen fraction to be $x_{\text{HI}} = 0.15^{+0.15}_{-0.15}$ at $z = 6.6$. Based on the halo occupation distribution models, we find that the $\gtrsim L^*$ LAEs are hosted by the dark-matter halos with the average mass of $\log(\langle M_{\text{h}} \rangle / M_{\odot}) = 11.1^{+0.2}_{-0.4}$ ($10.8^{+0.3}_{-0.5}$) at $z = 5.7$ (6.6) with a Ly α duty cycle of 1 % or less, where the results of $z = 6.6$ LAEs may be slightly biased, due to the increase of the clustering signal at the EoR. Our clustering analysis reveals the low-mass nature of $\gtrsim L^*$ LAEs at $z = 6 - 7$, and that these LAEs probably evolve into massive super- L^* galaxies in the present-day universe.

Key words: galaxies: formation — galaxies: high-redshift — cosmology: observations

1 Introduction

Ly α emitters (LAEs) are star-forming galaxies (and AGNs) with a strong Ly α emission line. In the 1960s, it was theoretically predicted that such galaxies are candidates of very young galaxies residing at $z \sim 10 - 30$ (Partridge & Peebles 1967). About 30 years after the predictions, deep observations identified a few LAEs around AGN regions at $z = 4.6$ (Hu & McMahon 1996) and $z = 2.4$ (Pascarelle et al. 1996). Subsequently, LAEs in blank fields are routinely found by deep and wide-field narrowband observations conducted under Hawaii Survey (Cowie & Hu 1998), Large Area Lyman Alpha Survey (Rhoads et al. 2000), and Subaru Surveys (e.g. Ouchi et al. 2003). These blank-field LAE surveys reveal various statistical properties of LAEs up to $z \sim 7$ including the evolution of Ly α luminosity functions (LFs; Malhotra & Rhoads 2004; Kashikawa et al. 2006; Ouchi et al. 2008; Deharveng et al. 2008; Cowie et al. 2010; Ouchi et al. 2010; Hu et al. 2010; Kashikawa et al. 2011; Konno et al. 2014; Matthee et al. 2015; Santos et al. 2016; Zheng et al. 2017; Ota et al. 2017). Moreover, multi-wavelength follow-up imaging and spectroscopy for LAEs reveal that the typical ($\sim L^*$) LAEs ($L_{\text{Ly}\alpha} = 10^{42} - 10^{43}$ erg s⁻¹) at $z \sim 2 - 3$ have a stellar

mass of $10^8 - 10^9 M_{\odot}$ (Gawiser et al. 2007; Hagen et al. 2014), a star-formation rate (SFR) of $\sim 10 M_{\odot}$ (Nakajima et al. 2012), and a gas-phase metallicity of $\sim 0.1 Z_{\odot}$ (Finkelstein et al. 2011; Guaita et al. 2013; Kojima et al. 2016). LAEs have strong high-ionization lines such as [OIII]5007, indicative of the high ionization state of the inter-stellar medium (ISM) given by intense ionizing radiation from young massive stars (Nakajima & Ouchi 2014). Outside the highly-ionized ISM, LAEs show diffuse extended Ly α halos in the circum-galactic medium (CGM) up to a few 10 kpc (Hayashino et al. 2004; Steidel et al. 2011). The bright Ly α halos extending over a few hundred kpc are known as Ly α blobs whose total Ly α luminosities are $\sim 10^{44}$ erg s⁻¹ (Steidel et al. 2000; Matsuda et al. 2004, cf. Saito et al. 2006), more than an order of magnitude brighter than the diffuse Ly α halos (Momose et al. 2014; Momose et al. 2016). Deep spectroscopic observations identify large spatial overdensities of LAEs up to $z \sim 6$ (Shimasaku et al. 2003; Ouchi et al. 2005a) that are possibly progenitors of massive galaxy clusters found today. Recent deep spectroscopy also detect strong Ly α emission of ~ 10 LAEs at $z = 7.0 - 8.7$, pushing the redshift frontier of LAEs, to date (e.g. Pentericci et al. 2011; Ono et al. 2012; Shibuya et al. 2012; Finkelstein et al. 2013; Schenker et

al. 2014; Oesch et al. 2015; Zitrin et al. 2015).

There are three major scientific goals in recent LAE studies. The first goal is characterizing the nature of low-mass young galaxies at high- z . Because LAEs are low stellar mass galaxies with strong Ly α indicative of a starburst with young massive stars producing a large amount of ionizing photons (Ouchi et al. 2013; Sobral et al. 2015; Stark et al. 2015), LAEs are used as probes of young galaxies. This motivation is the same as the one of the original predictions of LAEs given by Partridge & Peebles (1967). The second goal is to understand the density and dynamics of H I clouds in the ISM and the CGM of star-forming galaxies. Due to the resonance nature of Ly α emission, Ly α photons are scattered by H I gas in the ISM and the CGM, and the dynamical properties of Ly α sources are not simply understood with the observed Ly α velocity fields. Instead, both the density and kinematics of H I gas in the ISM and the CGM are encoded in the observed Ly α line velocity and spatial profiles. The combination of the Ly α line profile observations and models provide important information about the H I gas of the ISM and the CGM (Verhamme et al. 2008; Zheng et al. 2011; Shibuya et al. 2014; Hashimoto et al. 2015; Momose et al. 2016). The third goal is to reveal the cosmic reionization history and properties. Due to the strong damping absorption of Ly α by the IGM H I gas at the epoch of reionization (EoR; $z > 6$), Ly α emission of LAEs are absorbed in the partially neutral IGM. The Ly α absorption depress the observed Ly α luminosities of LAEs, which make a decrease of the Ly α LF towards the early stage of the EoR (Malhotra & Rhoads 2004; Kashikawa et al. 2006; Ouchi et al. 2010; Hu et al. 2010; Kashikawa et al. 2011; Santos et al. 2016; Ota et al. 2017). Moreover, the clustering signal of observed LAEs is boosted by the existence of the ionized bubbles (Furlanetto et al. 2006; McQuinn et al. 2007; Ouchi et al. 2010), because the Ly α absorption is selectively weak for LAEs residing in the ionized bubbles of the IGM at the EoR. The Ly α LFs and clustering of LAEs are important quantities to characterize the cosmic reionization history and ionized bubble topologies at the EoR.

There are three new large instruments that are used for LAE observations; VLT/Multi-Unit Spectroscopic Explorer (MUSE; Bacon et al. 2010), Hobby-Eberly Telescope Dark Energy Experiment/Visible Integral-Field Replicable Unit Spectrograph (HETDEX/VIRUS; Hill et al. 2012), and Subaru/Hyper Suprime-Cam (HSC; Miyazaki et al. 2017). These three instruments can cover the complementary parameter space of LAEs in redshift, depth, and survey volume. Specifically, Subaru/HSC has a capability to take large-area ($> 10 \text{ deg}^2$) deep images with the custom-made narrowbands (Section 2) targeting LAEs at $z \sim 2 - 7$. The combination of Subaru/HSC imaging and deep follow-up spectroscopy allows us to address the key issues of LAEs for accomplishing the three major goals described above.

One of the most unique studies realized with Subaru/HSC is clustering of LAEs at the EoR (i.e. $z \gtrsim 6$) that require high-sensitivity observations over a large area of the sky, as we show in this study. LAE clustering signals depend on the hosting dark-matter halo properties of LAEs, and the distribution of the patchy ionized IGM (i.e. ionized bubbles) that allows Ly α photons to escape from the partially neutral IGM at the EoR (Furlanetto et al. 2006; McQuinn et al. 2007; Ouchi et al. 2010). Theoretical models suggest that a Ly α LF measurement, a popular statistical quantity of LAEs, has a degeneracy between the Ly α escape fraction $f_{\text{esc}}^{\text{Ly}\alpha}$ (a flux ratio of observed to intrinsic Ly α emission; Le Delliou et al. 2006; Mao et al. 2007; Kobayashi et al. 2010) and duty cycle $f_{\text{duty}}^{\text{LAE}}$ (an abundance ratio of Ly α emitting galaxies to dark-matter haloes; Nagamine et al. 2010). Moreover, at the EoR, there is another degeneracy between the ionized bubble topology and neutral hydrogen fraction x_{HI} of the IGM (Kakiichi et al. 2016). Theoretical studies show that these degeneracies can be resolved with the combination of Ly α LF and clustering measurements (e.g. Nagamine et al. 2010; Sobacchi & Mesinger 2015; Hutter et al. 2015; Kakiichi et al. 2016). The LAE samples at the post EoR, e.g. $z = 5.7$, (the EoR, e.g. $z = 6.6$) are useful to determine $f_{\text{esc}}^{\text{Ly}\alpha}$ and $f_{\text{duty}}^{\text{LAE}}$.

In this paper, we describe our narrowband filters and the program strategy of the HSC LAE studies named 'Systematic Identification of LAEs for Visible Exploration and Reionization Research Using Subaru HSC' (SILVERRUSH; Section 2), and present our LAE samples (Section 3). We obtain measurements of LAE clustering (Section 4) that are calculated with the early samples of HSC LAEs at $z = 5.7$ and 6.6 (Shibuya et al. 2017a) based on the Hyper Suprime-Cam Subaru Strategic Program (SSP; HSC et al.) data whose first data release is presented in Aihara et al. (2017). Based on the LAE clustering measurements, we discuss cosmic reionization history and dark-matter halo properties of LAEs by the comparison with the Λ CDM structure formation models in Section 5. Throughout this paper, magnitudes are in the AB system. We adopt a cosmology parameter set of $(h, \Omega_m, \Omega_\Lambda, n_s, \sigma_8) = (0.7, 0.3, 0.7, 1.0, 0.8)$ consistent with the latest Planck results (Planck Collaboration et al. 2016).

2 Narrowband Filters and the Program Strategy for the LAE Studies

In our LAE studies, we use four custom-made narrowband filters that are fabricated for the HSC SSP survey. We design the HSC narrowband filters targeting the OH sky windows at 816, 921, and 1010 nm that correspond to NB816 (PI: Y. Taniguchi), NB921 (PI: M. Ouchi), and NB101 (PI: K. Shimasaku) filters identifying the redshifted Ly α of LAEs at $z = 5.7, 6.6$, and 7.3 , respectively. These three narrowband filters densely cover

LAEs from the heart of the EoR to the post-EoR. Another HSC narrowband filter is *NB387* (PI: K. Shimasaku) whose central wavelength is 387 nm. The *NB387* band is the bluest narrowband among the existing HSC filters, targeting the lowest redshift LAEs identified by the HSC observations. The central wavelength of 387 nm is specifically chosen, because this band identifies LAEs at $z = 2.2$ whose major strong lines of [OII]3727 and H α 6563 fall in the OH sky windows of 1.19 and $2.10\mu\text{m}$, respectively. The other major strong lines of H β 4861 and [OIII]5007 of $z = 2.2$ LAEs are placed at the *H* band, where the effects of the OH sky emission are unavoidable, due to no clear OH windows.

We carefully determine the full width at half maximum (FWHM) value for each narrowband filter transmission curve. First, we determine the FWHM of *NB921* that properly covers a clear OH window at the reddest band, allowing the typical transmission curve errors of the filter fabrication¹. We aim to accomplish the same detection limit of the rest-frame Ly α equivalent width EW_0 in our samples of LAEs at $z = 2.2$, 5.7, and 6.6. An observed-frame Ly α equivalent width EW_{obs} has the relation of $EW_{\text{obs}} = (1 + z)EW_0$. Because a narrowband flux excess is proportional (inversely-proportional) to EW_{obs} (a narrowband FWHM value), we scale the FWHM value of the *NB921* band ($FWHM_{\text{NB921}}$) by $(1 + z)$ to design the FWHM values of *NB387* ($FWHM_{\text{NB387}}$) and *NB816* ($FWHM_{\text{NB816}}$). More specifically, the designed FWHM values keep the relations of $FWHM_{\text{NB387}} = FWHM_{\text{NB921}}(1 + 2.18)/(1 + 6.58)$ and $FWHM_{\text{NB816}} = FWHM_{\text{NB921}}(1 + 5.71)/(1 + 6.58)$, where the numbers of 2.18, 5.71, and 6.58 correspond to the redshifts of the Ly α lines (121.567nm) falling in the centers of the *NB387*, *NB816*, and *NB921* bandpasses, respectively. Here, the FWHM of the *NB101* band does not follow this scaling relation. Instead, we choose an FWHM that is the narrowest limit that can be reasonably accomplished by the present technology of the HSC narrowband filter fabrication. This is because Ly α lines of the *NB101* LAEs fall in the wavelength range where the HSC imaging cannot reach a very deep magnitude limit, due to the relatively low CCD quantum efficiency and the unclear OH window. In this way, we obtain the designed specifications of (central wavelength, FWHM wavelength) = (387.0nm, 5.5nm) for *NB387*, (816.0nm, 11.6nm) for *NB816*, (921.0nm, 13.1nm) for *NB921*, and (1009.5nm, 9.0nm) for *NB101*.

The HSC narrowband filters are made of a B270 or quartz glass with multi-layer interferometric coatings that make the sharp cut-on and cut-off bandpasses for the narrowband filters. The diameter of the HSC narrowband filter is large, 600 mm.

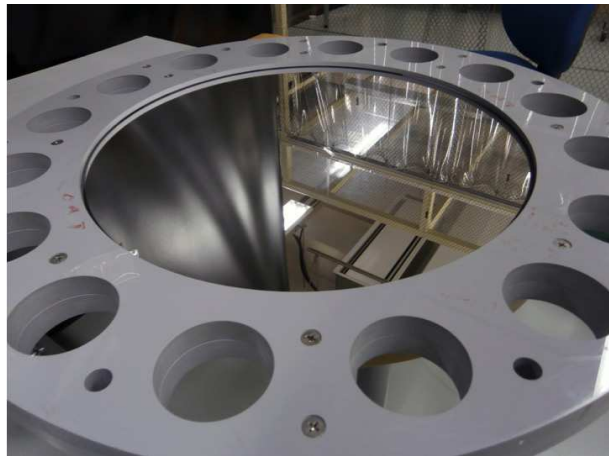


Fig. 1. HSC *NB921* filter in a filter holder.

Although uniform coatings are key to accomplish the spatially-homogeneous transmission of the narrowband filters, small non-uniformities are included in the fabrication processes, which give the filter characterization slightly different from the design. Nevertheless, we have tried to make the coating distribution as uniformly as possible to achieve spatially-homogeneous transmission curves for the narrowband filters. The picture of *NB921* is shown in Figure 1.

Figures 2 and 3 present the transmission curves of the HSC *NB816* and *NB921* filters that are used in the HSC first-data release (Aihara et al. 2017). We measure the transmission curves at 21 points over the 600mm-diameter circular filter. The detectors of the camera need transmission of the circular filter from the center $r = 0$ to the radius of $r = 280$ mm. Facing on the filter, we define the angle of 0 deg for the arbitrary direction from the filter center to the edge. On the angle of 0 deg, we measure transmission curves at the 5 positions of $r = 50, 100, 150, 200$, and 270 mm. We change the angle to 90, 180, and 270 deg for the counter clockwise direction, and obtain the transmission curves at the 20 positions ($= 5 \times 4$). Including the measurement at the center ($r = 0$ mm), we have the transmission curves at a total of 21 positions. Note that the measurement position of *NB921* is slightly different from the one of *NB816*. The $r = 270$ mm position is replaced with $r = 265$ mm for the *NB921* filter. We find that the area-weighted average central wavelength and FWHM of *NB816* (*NB921*) are 817.7 nm and 11.3 nm (921.5 nm and 13.5 nm), respectively, and that the central-position central wavelength and FWHM of *NB816* (*NB921*) are 816.8 nm and 11.0 nm (920.5 nm and 13.3 nm), respectively. At any positions within $r \leq 265$ mm, the peak transmissions of *NB816* and *NB921* are high, $> 90\%$. The deviations of the central and FWHM wavelengths are typically within $\simeq 0.3\%$ and $\simeq 10\%$, respectively.

Using the HSC narrowband filters, we study LAEs at $z = 2.2$, 5.7 and 6.6 (7.3) over the large areas of 26 (3.5) deg² that are

¹ There are some more OH windows redder than 921 nm, which include the 1010-nm window for the *NB101* filter. However, these OH windows in the red band are contaminated by moderately strong OH lines, unlike the one of 921 nm.

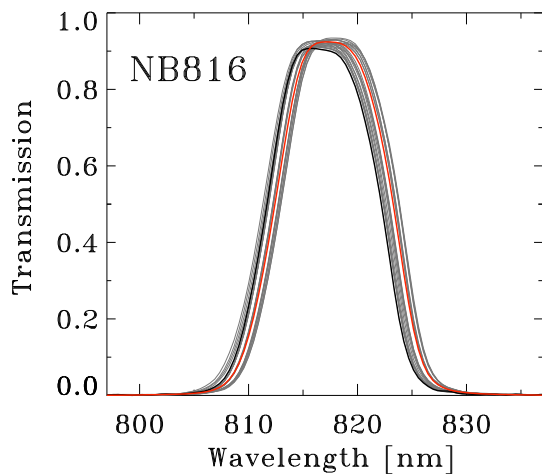


Fig. 2. Filter transmission curves of *NB816*. The gray lines present the transmission curves at the 21 positions (see text). The black line is the same as the gray lines, but the transmission curve at the central position. The red line represents the area-averaged mean transmission curve that is shown in the Subaru website²

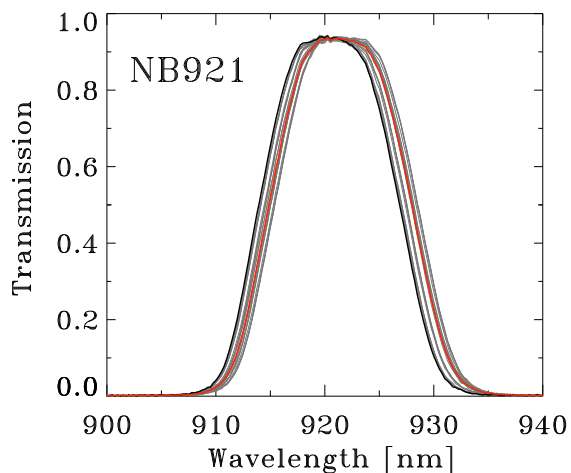


Fig. 3. Same as Figure 2, but for *NB921*.

about an order of magnitude larger than those of the previous studies for a given redshift. Exploiting samples of $z = 2.2$ and 5.7 LAEs, we study evolution of LAEs at $z = 2.2 - 5.7$, from the lowest redshift accessible by ground-based observations ($z \sim 2$) to the high- z edge of the post reionization epoch ($z \sim 6$). The LAEs at three redshifts of $z = 5.7$, 6.6 , and 7.3 allow us to study evolution of galaxy formation as well as cosmic reionization with the $\text{Ly}\alpha$ damping wing absorption of the neutral IGM. The LAEs at the post reionization epoch of $z = 5.7$ play a role of the baseline for the properties of LAEs with no cosmic reionization effects given by the IGM $\text{Ly}\alpha$ damping wing absorption. The comparisons of $z = 5.7$ and 6.6 LAEs over the 26 deg^2 sky provide large statistical results, while the $z = 7.3$ LAEs in the moderately large 3.5 deg^2 area allows us to investigate galaxy formation and cosmic reionization at the heart of EoR. Based on

the data sets of the HSC SSP survey (see Aihara et al. 2017 for the details of the first-data release) and our extensive spectroscopic follow up observations with Subaru, Keck, and Magellan telescopes, we start the program named SILVERRUSH (Section 1). This program is one of the twin programs. The other program is the study for dropouts, Great Optically Luminous Dropout Research Using Subaru HSC (GOLDRUSH), that is detailed in Ono et al. (2017), Harikane et al. (2017), and Toshikawa et al. (2017).

In a series of SILVERRUSH papers, we present the SILVERRUSH program strategy (this paper), LAE sample selections (Shibuya et al. 2017a), and spectroscopic follow-up observations (Shibuya et al. 2017b), $\text{Ly}\alpha$ LF evolution (Konno et al. 2017), LAE clustering evolution (this paper), and the comparisons with numerical simulation results (Inoue et al. 2017). These are early papers of the SILVERRUSH program whose observations are still underway. In these early papers, we present the results of the LAE studies based on the images taken until 2016 April that include neither *NB387* (for $z = 2.2$ LAEs) nor *NB101* (for $z = 7.3$ LAEs) data, but only *NB816* and *NB921* data for $z = 5.7$ and 6.6 LAEs, respectively (Section 3). Here, we aim that SILVERRUSH results can serve as the baselines of LAE properties useful for the on-going LAE studies including MUSE, HETDEX, and the forthcoming $z > 7$ galaxy studies of James Webb Space Telescope (JWST) and extremely large telescopes (ELTs).

3 Observations and Sample

The HSC SSP survey started observations in March 2014, taking deep broadband and narrowband images on large areas of the sky (PI: S. Miyazaki). In our study, we use the HSC SSP survey (HSC et al. in prep) data taken until 2016 April with two narrowbands (*NB816* and *NB921*) and five broadbands (*grizy*) useful for our LAE studies. Because the data of *NB387* and *NB101* (for detections of LAEs at $z = 2.2$ and 7.3) are not taken until 2016 April, we present the results of imaging with the two narrowband *NB816* and *NB921* (for LAEs at $z = 5.7$ and 6.6) whose observations have been partly conducted. The data are reduced with the HSC pipeline software, hscPipe version 4.0.2 (Bosch et al. 2017). The 5σ depths of the imaging data are typically $\simeq 25 - 25.5$ and $\simeq 26 - 27$ magnitudes in narrowbands and broadbands, respectively (see Shibuya et al. 2017a for more details). Note that the HSC SSP survey data set used in this study is notably larger than the one of the first-data release (Aihara et al. 2017) that is composed of images taken only in 2014 March and 2015 November.

Our LAEs are selected with the combinations of broadband and narrowband colors down to the 5σ detection limits. The LAEs should have a narrowband excess, the existence of Gunn-Peterson trough, and no detection of blue continuum fluxes. The

Table 1. LAE Samples and the Clustering Measurements

z	$L_{\text{Ly}\alpha}^{\text{th}}$ ($10^{42} \text{ erg s}^{-1}$)	n_g (10^{-5} Mpc^{-3})	N	IC (10^{-3})	r_0 ($h_{100}^{-1} \text{ Mpc}$)	b_{avg}	r_0^{max} ($h_{100}^{-1} \text{ Mpc}$)	$b_{\text{avg}}^{\text{max}}$	χ^2/dof
(1)	(2)	(3)	(4)	(5)	(6)	(7)	(8)	(9)	(10)
5.7	6.3	7.3	959 [†]	1.83	$3.01^{+0.35}_{-0.35}$	4.13 ± 0.17	$4.47^{+0.52}_{-0.52}$	5.90 ± 0.24	5.69/5
6.6	7.9	2.4	873	1.35	$2.66^{+0.49}_{-0.70}$	4.54 ± 0.63	$3.95^{+0.73}_{-1.04}$	6.49 ± 0.90	2.70/2

For comparison, r_0 is expressed with h_{100} . [†] The number including sources in D-ELAIS-N1.

color selection criteria are similar to those of Ouchi et al. 2008 and Ouchi et al. 2010 that are defined as

$$i - NB816 \geq 1.2 \text{ and } g > g_{3\sigma} \text{ and}$$

$$[(r \leq r_{3\sigma} \text{ and } r - i \geq 1.0) \text{ or } (r > r_{3\sigma})] \quad (1)$$

and

$$z - NB921 \geq 1.0 \text{ and } g > g_{3\sigma} \text{ and } r > r_{3\sigma} \text{ and}$$

$$[(z \leq z_{3\sigma} \text{ and } i - z \geq 1.3) \text{ or } (z > z_{3\sigma})] \quad (2)$$

for $z = 5.7$ and 6.6 LAEs, respectively, where $g_{3\sigma}$ ($r_{3\sigma}$) is the 3σ limiting magnitude of g (r) band that ensures no detection of a continuum bluer than the Lyman break. Similarly, $z_{3\sigma}$ is the 3σ detection limit of z band. After applying the candidate screening on the basis of hscPipe parameters+flags and visual inspection, we obtain a total of 2,354 LAEs (1,081 and 1,273 LAEs at $z = 5.7$ and 6.6 , respectively) from the LAE ALL catalogs (Shibuya et al. 2017a). We investigate the 2,354 LAEs, and make homogeneous samples over the survey areas that consist of 1,832 LAEs (959 and 873 LAEs at $z = 5.7$ and 6.6 , respectively) with a common narrowband limiting magnitude of $NB816 < 25.0$ or $NB921 < 25.0$ that is surely brighter than the 5σ detection levels. The homogenous samples of $z = 5.7$ and 6.6 LAEs have very similar threshold luminosities (the rest-frame equivalent width) of $L_{\text{Ly}\alpha}^{\text{th}} > 6.3 \times 10^{42}$ and $7.9 \times 10^{42} \text{ erg s}^{-1}$ ($EW_0 \gtrsim 20\text{\AA}$) at $z = 5.7$ and 6.6 , respectively. The threshold luminosities correspond to $\simeq L^*$ luminosities (e.g. Ouchi et al. 2008; Ouchi et al. 2010; Konno et al. 2017). The LAE sample selection is detailed in Shibuya et al. (2017a).

These LAEs are found in a total of 13.8 (21.2) deg^2 area consisting of the fields named D-ELAIS-N1, D-DEEP2-3, UD-COSMOS, and UD-SXDS for the $z = 5.7$ LAE sample (D-ELAIS-N1, D-DEEP2-3, D-COSMOS, UD-COSMOS, and UD-SXDS for the $z = 6.6$ LAE sample). Because, for the $z = 5.7$ and 6.6 LAE samples, the redshift ranges are $z = 5.726 \pm 0.046$ and $z = 6.580 \pm 0.056$ in the case that top-hat selection functions of LAEs with the FWHMs of the narrowband filters are assumed, the total survey volumes covered with the narrowband transmission are 1.2×10^7 and 1.9×10^7 comoving Mpc^3 at $z = 5.7$ and 6.6 , respectively. Note that the total areas of 13.8 and 21.2 deg^2 for the $z = 5.7$ and 6.6 samples correspond to 0.3 and 0.5 comoving Gpc^2 areas, respectively. These large survey areas allow us to study average properties of LAEs at $z = 6 - 7$ whose observabilities are influenced by

patchy (10 – 100 Mpc) ionized bubbles probably existing at the end of the EoR (Furlanetto et al. 2006).

In our LAE samples, a total of 97 LAEs at $z = 5.7$ and 6.6 are confirmed by our spectroscopic observations and the cross-matching of the existing spectra (Shibuya et al. 2017b). Because there are 81 LAE candidates whose spectroscopic identifications are obtained by our past and present programs, we estimate contamination rates of our LAE samples with these 81 LAE candidates that consist of 53 and 28 LAEs at $z = 5.7$ and 6.6 , respectively. We find 4 out of 53 (4 out of 28) candidates are foreground contamination objects, and estimate the contamination rates to be $\sim 8\%$ and $\sim 14\%$ for the samples of LAEs at $z = 5.7$ and 6.6 , respectively. We also investigate contamination rates of bright LAEs that are brighter than 24 magnitudes in the narrowband. There are 6 and 12 bright LAE candidates with spectroscopic identifications. The spectroscopic results indicate that 1 out of 6 (4 out of 12) LAE candidates are foreground interlopers, which correspond to the contamination rate of $\sim 17\%$ ($\sim 33\%$) for the sample of LAEs at $z = 5.7$ (6.6). Although the contamination rates depend on magnitude, the contamination rates indicated by the spectroscopic confirmation range in around 0 – 30% in our $z = 5.7$ and 6.6 LAE samples. Although the contamination rates include large uncertainties due to the small number of our spectroscopically confirmed sources at this early stage of our LAE studies, we assume that the contamination rates are 0 – 30% in our LAE samples that are used in our analysis below.

4 Clustering Analysis and Results

Figures 4 and 5 present the sky distribution of the LAEs at $z = 5.7$ and 6.6 , respectively. In Figure 4, we find that the density of $z = 5.7$ LAEs in the D-ELAIS-N1 field is largely biased to the southern region, considering the possibilities of the detection incompleteness and the real large overdensity. We have carefully investigated our D-ELAIS-N1 images, but found no significant spatial fluctuations of the detection completeness produced by the inhomogeneity of the data handling and the data qualities including depths and seeing sizes. However, there remain the possibilities that unknown effects of the data reduction may produce the large overdensity. Because the origin of this large overdensity is still unknown, we do not use the data of D-ELAIS-N1 in this study. Instead, we discuss this overdensity

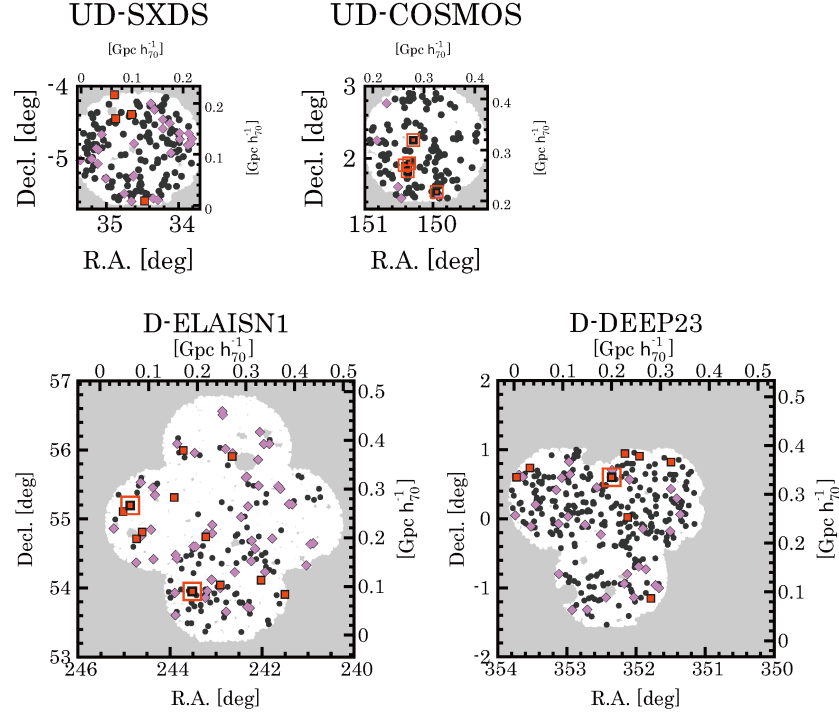


Fig. 4. Sky distribution of the LAEs at $z = 5.7$. The red squares, magenta diamonds, and black circles represent positions of narrowband bright (< 23.5 mag), medium-bright ($23.5 - 24.0$ mag), and faint ($24.0 - 25.0$ mag) LAEs, respectively. The large red open square indicates the LAEs with spatially extended $\text{Ly}\alpha$ emission (Shibuya et al. 2017b). The gray shades denote either the areas with no HSC data or the masked regions with a bad data quality. The scale on the map is marked in angles (degrees) and the projected distances (comoving megaparsecs).

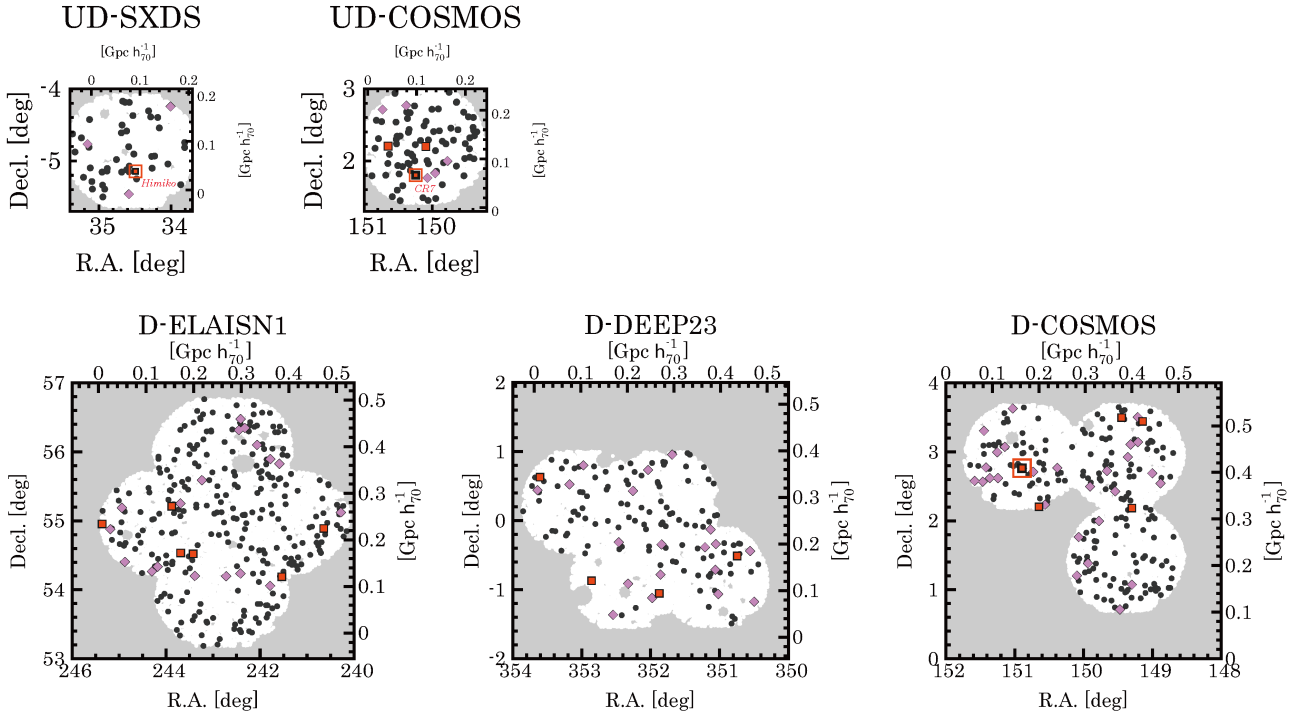


Fig. 5. Same as Figure 4, but for the LAEs $z = 6.6$. The large red open squares indicate the LAEs with spatially extended $\text{Ly}\alpha$ emission including Himiko (Ouchi et al. 2009a) and CR7 (Sobral et al. 2015). See Shibuya et al. (2017b) for more details.

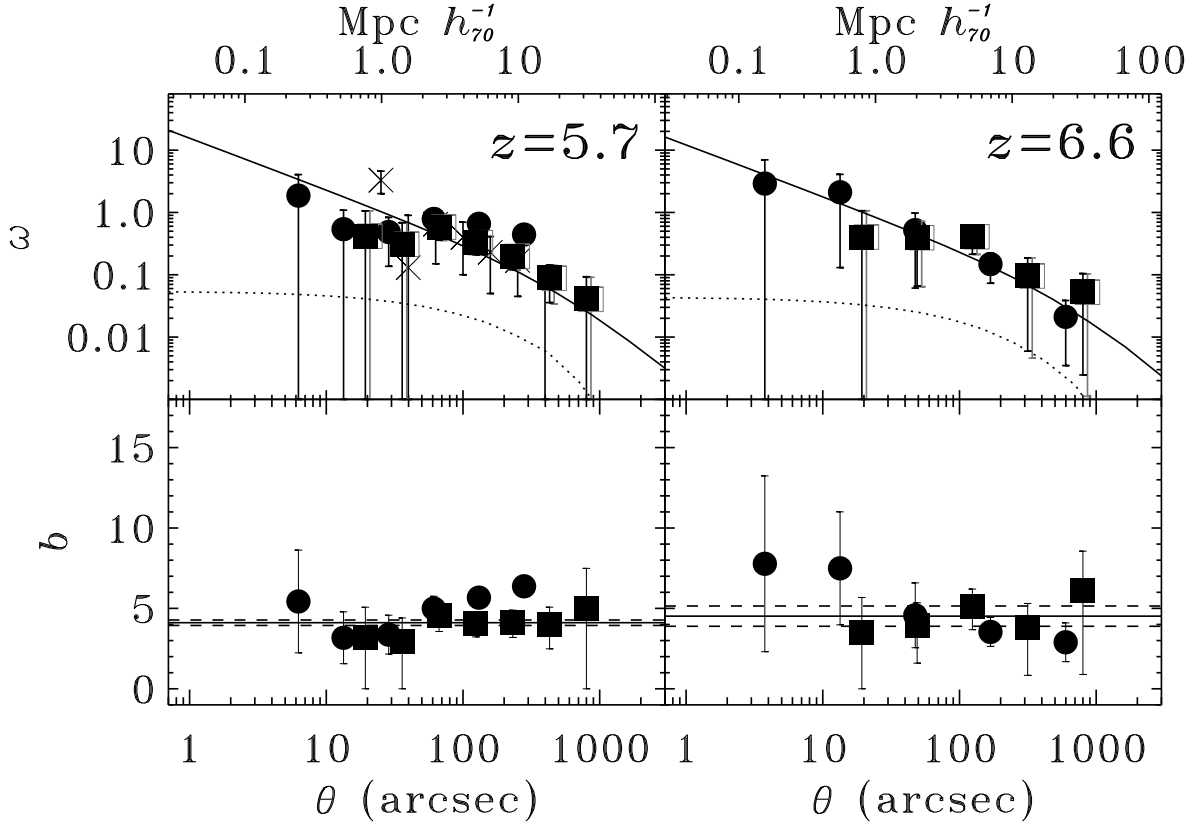


Fig. 6. Angular correlation function (ACF) and bias of the LAEs at $z = 5.7$ (left) and 6.6 (right). The top and bottom panels show the ACFs and the bias. The black-filled and gray-open squares represent the ACFs of our LAEs with and without the IC correction, respectively, while the filled circles denote the ACFs with the IC correction derived by Ouchi et al. (2010). For presentation purposes, we slightly shift the gray open squares along the abscissa. In the top panels, the solid and dotted lines present the best-fit power-law functions of our ACFs and the ACFs of the underlying dark matter predicted by the linear theory (e.g. Peacock & Dodds 1994). Because the power-law spatial correlation function is projected on sky with the method in Simon (2007), the best-fit power-law functions are curves. In the bottom panels, the solid and dashed lines indicate the average bias and the 1σ error values, respectively. The crosses in the top left panel show the ACFs obtained by Murayama et al. (2007). The top axis denotes the projected distance in comoving megaparsecs.

in R. Higuchi et al. (in preparation). We thus use the remaining 734 LAEs at $z = 5.7$ in our analysis.

We quantify clustering properties based on the measurements of the angular correlation functions in the following sections.

4.1 Angular Correlation Function

We derive angular two-point correlation functions (ACFs) of our LAEs in the same manner as Ouchi et al. (2003), Ouchi et al. (2005b), Ouchi et al. (2010), and Harikane et al. (2016). We use the estimator of Landy & Szalay (1993),

$$\omega_{\text{obs}}(\theta) = \frac{DD(\theta) - 2DR(\theta) + RR(\theta)}{RR(\theta)}, \quad (3)$$

where $DD(\theta)$, $DR(\theta)$, and $RR(\theta)$ are numbers of galaxy-galaxy, galaxy-random, and random-random pairs normalized by the total number of pairs in each of the samples of the pairs. We use the random catalog (Coupon et al. in preparation) whose surface number density is 100 arcmin^{-2} . The random catalog has the geometrical constraint same as the one of our LAEs,

representing our survey areas. Statistical errors are estimated with Jackknife resampling with subsamples each of which has a $\sim 1000^2 \text{ arcsec}^2$ area. Figure 6 shows the observed ACFs $\omega_{\text{obs}}(\theta)$ of our LAEs at $z = 5.7$ and 6.6 . The ACF measurements cover the scale of $\sim 1 - 100$ comoving Mpc that is indicated in the upper axes of Figure 6. We find that these ACFs are consistent with those obtained with the previous Subaru/Suprime-Cam data (Ouchi et al. 2010), and that our present HSC data provide the large-scale ACFs with uncertainties smaller than those of the previous data.

Although our survey area is large, we evaluate the integral constraint IC (Groth & Peebles 1977). The IC value corresponds to the observational offset in $\omega_{\text{obs}}(\theta)$ originated by a limited survey area. Including the correction for the number of objects in the sample, N , the true ACF is given by

$$\omega(\theta) = \omega_{\text{obs}}(\theta) + \text{IC} + \frac{1}{N}, \quad (4)$$

We evaluate the integral constraint with

$$\text{IC} = \frac{\sum_i RR(\theta_i) \omega(\theta_i)}{\sum_i RR(\theta_i)}, \quad (5)$$

We adopt the model ACF of Simon (2007) for the function of $\omega(\theta)$ that is detailed in Section 4.2. We show IC values in Table 1, and plot the ACFs corrected for IC in Figure 6. Note that the IC values are very small, because our survey areas are very large.

A clustering signal of galaxies is diluted by contamination objects in a galaxy sample. If the galaxy sample includes randomly-distributed contamination objects with a fraction f_c , the value of the ACF is reduced by a factor of $(1 - f_c)^2$. The ACF corrected for the randomly-distributed contamination ω_{\max} is written as

$$\omega_{\max} = \frac{\omega}{(1 - f_c)^2}. \quad (6)$$

This is the maximum reduction of the ACF, because the real contamination objects are not randomly distributed but spatially correlated. For reference, we evaluate the possible maximum values of ω_{\max} , using the contamination fraction whose upper limit is $f_c = 0.3$ (Section 3).

4.2 Correlation Length and Bias

We fit the ACFs with a simple power law model of the spatial correlation function,

$$\xi(r) = \left(\frac{r}{r_0}\right)^{-\gamma}, \quad (7)$$

where γ , r_0 , and r are the slope of the power law, the correlation length, and the spatial separation between two galaxies, respectively. The spatial correlation function is related to the ACF with the Limber equation (Peebles 1980; Efsthathiou et al. 1991) that is an integral equation of the (three-dimensional) spatial correlation function connecting with the (two-dimensional) ACF. However, Simon (2007) claims that the Limber equation does not provide accurate values in a very large separation of galaxies whose redshift-distribution distance is narrower than the transverse distance in the case such for narrowband-selected LAEs. We thus adopt the method that Simon (2007) suggests, and derive r_0 of our LAEs, fitting the power-law functions to our ACFs. Because no meaningful constraints on γ are obtained with the present samples, we adopt the fiducial γ value of $\gamma = 1.8$ that is adopted in the previous clustering analyses for LAEs (Ouchi et al. 2003; Gawiser et al. 2007; Kovač et al. 2007; Ouchi et al. 2010). To investigate the dependences of our results on the value of γ , we also use the other fixed γ values of $\gamma = 1.6$ and 2.0 that bracket the possible range of the power-law index of high- z galaxies at $z \sim 4-6$ (Lee et al. 2006; McLure et al. 2009). We have found that neither r_0 nor bias values changes over 10%, and that r_0 and bias values fall well within the errors. Here, we use the redshift distribution of our LAEs estimated with the narrowband transmission curve. The best-fit power-law functions are presented in Figure 6. The correlation lengths thus obtained are $r_0 = 3.01^{+0.35}_{-0.35}$ and $2.66^{+0.49}_{-0.70} h_{100}^{-1}$ Mpc for

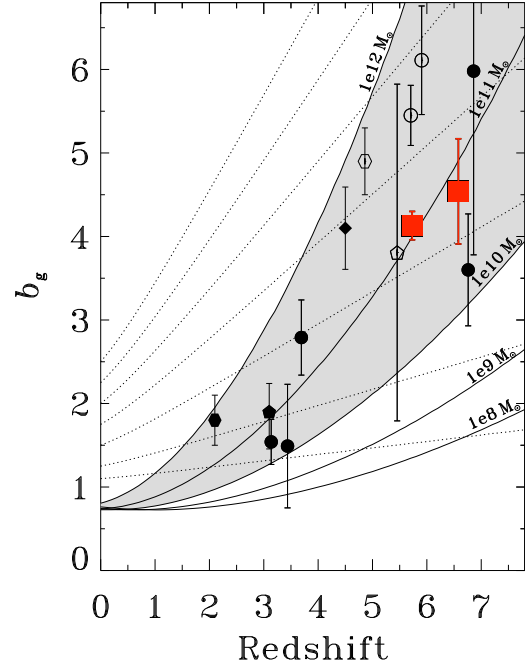


Fig. 7. Bias of $\gtrsim L^*$ LAEs as a function of redshift. The red squares represent bias of our LAEs at $z = 5.7$ and 6.6 , while the filled circles denote those of LAEs obtained in Ouchi et al. (2010). The open circles, pentagon, and hexagon indicate LAE bias values obtained by Ouchi et al. (2005a), and Ouchi et al. (2003), respectively. The filled hexagon, pentagon, and diamond are LAE bias values measured by Guaita et al. (2010), Gawiser et al. (2007), and Kovač et al. (2007), respectively. For the previous study results, we correct for the difference of σ_8 . To clarify the bias measurements, we give small offsets along the abscissa axis to the data points of the previous studies. The solid lines indicate bias of dark-matter halos with a halo mass of 10^8 , 10^9 , 10^{10} , 10^{11} , and $10^{12} M_\odot$ in the case of one-to-one correspondence between galaxies and dark-matter halos (Ouchi et al. 2010). The gray region shows the dark-matter halo mass range of $10^{10} - 10^{12} M_\odot$. The dotted lines are evolutionary tracks of bias in the case of the galaxy-conserving model (eq. 13).

LAEs at $z = 5.7$ and 6.6 , respectively, that are summarized in Table 1. To make comparisons with the previous results, we express the correlation lengths with h_{100} , the Hubble constant in units of 100 km s^{-1} , instead of 70 km s^{-1} . Table 1 also shows the upper limit of the correlation length, r_0^{\max} , that is given by

$$r_0^{\max} = r_0 \left(\frac{1}{1 - f_c} \right)^{2/\gamma}. \quad (8)$$

We obtain $r_0^{\max} = 4.47^{+0.52}_{-0.52}$ and $3.95^{+0.73}_{-1.04} h_{100}^{-1}$ Mpc for our $z = 5.7$ and 6.6 LAEs, respectively.

These correlation length values are consistent with the previous measurements within the errors. Ouchi et al. (2010) obtain (r_0, r_0^{\max}) of $(3.12^{+0.33}_{-0.36}, 4.30^{+0.45}_{-0.50})$ and $(2.31^{+0.65}_{-0.85}, 3.60^{+1.02}_{-1.32})$ for LAEs at $z = 5.7$ and 6.6 , respectively.

In the framework of the Λ CDM model, the galaxy-dark matter bias is defined by

$$b_g(\theta)^2 \equiv \omega(\theta)/\omega_{\text{dm}}(\theta), \quad (9)$$

where $\omega_{\text{dm}}(\theta)$ is the ACF of dark-matter predicted by the linear theory model (e.g. Peacock & Dodds 1994). The model calculations are made with the same survey volumes as those of our LAE samples. Note that b_g is the bias value equivalent to the one given by the three-dimensional spatial correlation functions, $b_g^2 = \xi(r)/\xi_{\text{dm}}(r)$, where $\xi_{\text{dm}}(r)$ is the spatial correlation function of dark matter.

In Figure 6, the top and bottom panels show $\omega_{\text{dm}}(\theta)$ and $b_g(\theta)$, respectively. We estimate the average bias b_{avg} , averaging $b_g(\theta)$ with error weighting over the angular range presented in Figure 6. We also calculate the upper limits of bias values $b_{\text{avg}}^{\text{max}}$ with the maximal contamination correction that corresponds to A_{ω}^{max} (eq. 6; see Section 4.1). We obtain $b_{\text{avg}} = 4.13 \pm 0.17$ and 4.54 ± 0.63 ($b_{\text{avg}}^{\text{max}} = 5.90 \pm 0.24$ and 6.49 ± 0.90) for our $z = 5.7$ and 6.6 LAEs, respectively. We summarize b_{avg} and $b_{\text{avg}}^{\text{max}}$ values thus obtained in Table 1. We compare these bias values with those obtained in the previous studies. We find that the bias value of our LAEs are consistent with those derived by Ouchi et al. (2005a) and Ouchi et al. (2010) within the $\sim 1\sigma$ errors.

Figure 7 presents bias of LAEs as a function of redshift. In Figure 7, we plot bias measurements of LAEs at $z = 2 - 7$ derived in the previous studies. We have corrected these previous study measurements of b_g for the difference of σ_8 (Ouchi et al. 2010), and shown the corrected b_g values in Figure 7.

This work and the previous studies measure bias of LAEs whose Ly α -luminosity detection limits are similar, a few times $10^{42} \text{ erg s}^{-1}$ corresponding to $\sim L^*$ luminosities over $z \sim 2 - 7$ (e.g. Ouchi et al. 2008; Ouchi et al. 2010; Konno et al. 2016; Konno et al. 2017). Thus, we can omit the luminosity segregation effects in bias that depends on Ly α luminosity. Figure 7 indicates that the bias of $\gtrsim L^*$ LAEs significantly increases from $z \sim 2 - 3$ to $z \sim 6 - 7$. The physical origins of this increase are discussed in Section 5.

5 Discussion

5.1 Cosmic Reionization

5.1.1 Constraints on x_{HI} from the Clustering Results

Clustering signals of observed LAEs are strengthened by the patchy distribution of the neutral hydrogen at the EoR, because Ly α photons of LAEs in the ionized bubbles can selectively escape from the patchy neutral IGM with a small amount of Ly α damping wing absorption (Furlanetto et al. 2006; McQuinn et al. 2007; Lidz et al. 2009; Iliev et al. 2008; Sobacchi & Mesinger 2015). Based on the fact that the Gunn-Peterson optical depth largely increases at $z \sim 6$ (Fan et al. 2006), one would expect that the clustering amplitude of the observed LAEs increases from $z = 5.7$ (the ionized universe) to $z = 6.6$ (the partly-

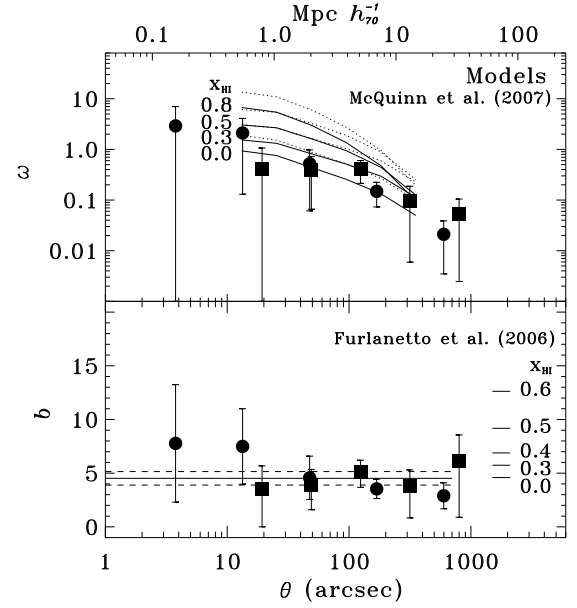


Fig. 8. Comparisons of the theoretical models with the ACF and bias measurements at $z = 6.6$. In the top (bottom) panel, the filled squares and circles denote the ACF (bias) measurements with the IC correction obtained by this work and Ouchi et al. (2010), respectively, which are the same as those shown in the top (bottom) right panel of Figure 6. *Top*: The solid and dotted lines represent the McQuinn et al.'s (2007) models of $z = 6.6$ LAEs with a dark-matter halo masses of $3 \times 10^9 M_{\odot}$ and $3 \times 10^{10} M_{\odot}$, respectively. The model of $3 \times 10^9 M_{\odot}$ is the modification of the model of $3 \times 10^{10} M_{\odot}$ (see text). From the bottom to the top solid (dotted) lines, neutral hydrogen fractions of the IGM are $x_{\text{HI}} = 0.0, 0.3, 0.5$, and 0.8 . *Bottom*: The ticks at the right-hand side indicate bias values predicted by Furlanetto et al.'s (2006) models (see text). The solid and dashed lines indicate the average bias and the 1σ uncertainty values, respectively, that are the same as those shown in the bottom right panel of Figure 6.

neutral universe). Figure 7 indicates no significant rise of bias from $z = 5.7$ to 6.6 beyond the moderately small errors (i.e. by a factor of $\sim 20\%$). This result suggests that clustering of $z = 6.6$ LAEs is not largely affected by the cosmic reionization effects, where the bias evolution of the hosting dark-matter halos towards high- z may be also involved. Based on this bias evolution result, we place constraints on cosmic reionization parameters with the help of theoretical models. We compare our observational results with multiple theoretical models, because there is a possibility that our conclusions may depend on a model chosen for the comparisons. We thus try to avoid model-dependent conclusions as much as possible, and to obtain more objective interpretations for our observational results. Note that the arguments below follow those of Ouchi et al. (2010) with our HSC clustering measurements.

In the top panel of Figure 8, we compare our $z = 6.6$ LAE clustering measurements with those of theoretical predictions (McQuinn et al. 2007; Furlanetto et al. 2006). The model of McQuinn et al. (2007) is presented in the top panel of Figure 8. McQuinn et al. (2007) conduct radiative transfer simulations predicting clustering of LAEs at $z = 6.6$. Their models assign

a Ly α flux to a dark-matter halo whose mass is beyond a minimum dark-matter halo mass. We use the minimum dark-matter halo mass of our LAEs at the post-reionization epoch of $z = 5.7$ to estimate the intrinsic LAE clustering at $z = 6.6$, assuming no redshift evolution ($z = 5.7 - 6.6$) of the minimum dark-matter halo mass (Section 3). Although the minimum dark-matter halo mass is $3 \times 10^9 M_\odot$ for the $z = 5.7$ LAEs (Section 5.2), McQuinn et al. (2007) do not calculate the models of the minimum dark-matter halo mass as low as $3 \times 10^9 M_\odot$. We thus correct the angular correlation functions of the McQuinn et al.'s lowest mass ($3 \times 10^{10} M_\odot$) model for the difference between 3×10^{10} and $3 \times 10^9 M_\odot$, using eq. (9). Here we calculate the bias values of the 3×10^{10} and $3 \times 10^9 M_\odot$ cases with the best-fit halo model (Section 5.2) whose parameters are exactly the same as those determined at $z = 5.7$. In the top panel of Figure 8, we show the McQuinn et al.'s models for $3 \times 10^9 M_\odot$ with the correction, together with the original $3 \times 10^{10} M_\odot$ model. Because the McQuinn et al.'s models do not correct for the integral constraint, we do not compare the model predictions below $\omega \sim 0.1$, where the contribution of the integral-constraint correction term is large. The top panel of Figure 8 indicates that our $z = 6.6$ LAE data points fall in the range of $x_{\text{HI}} \simeq 0 - 0.3$, indicating $x_{\text{HI}} = 0.15 \pm 0.15$.

In the bottom panel of Figure 8, we compare our bias results with those of analytical models of Furlanetto et al. (2006) at $z = 6.6$. In this comparison, we adopt the bias values of the small-scale ($\simeq 1 - 10$ Mpc) of Furlanetto et al. (2006) that is similar to the major angular scale of our bias measurements. For the intrinsic bias value of the $z = 6.6$ LAEs, we use $b = 4.6$ that is obtained under the assumption of no evolution from $z = 5.7$ to 6.6 for the minimum dark-matter halo mass ($3 \times 10^9 M_\odot$) and the halo-model parameters (Section 5.2). The bottom panel of Figure 8 presents that our average-bias measurement agrees with the low x_{HI} models of Furlanetto et al. (2006), and suggests $x_{\text{HI}} \lesssim 0.13$ including the uncertainty of the average-bias measurement of the $z = 6.6$ LAEs.

The comparisons of our observational results with the models of McQuinn et al. (2007) and Furlanetto et al. (2006) indicate that the neutral hydrogen fraction at $z = 6.6$ falls in the range of $x_{\text{HI}} = 0.15^{+0.15}_{-0.15}$.

5.1.2 Cosmic Reionization History

Figure 9 shows our x_{HI} value of $x_{\text{HI}} = 0.15^{+0.15}_{-0.15}$ that is estimated with our LAE clustering measurements. This x_{HI} estimate suggests a moderate neutral hydrogen fraction at $z = 6.6$. In Figure 9, we also present various results of x_{HI} constrained by the similar LAE clustering analysis (Ouchi et al. 2010) and the independent x_{HI} estimates from QSO Gunn-Peterson absorptions (Fan et al. 2006) as well as Ly α damping wing (DW) absorption measurements of QSOs (Mortlock et al. 2011; Bolton et al. 2011), Gamma-ray bursts (GRBs; Totani

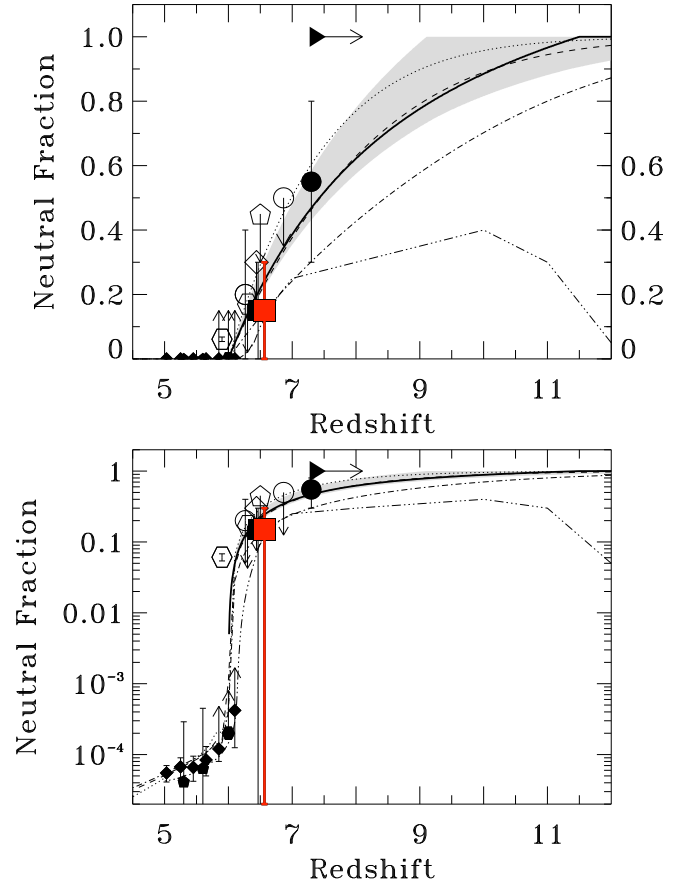


Fig. 9. Neutral hydrogen fraction x_{HI} of the IGM as a function of redshift. Note that the top and bottom panels are the same, but with an ordinate axis of linear and log scales, respectively. The red filled square is the x_{HI} estimate obtained by our HSC LAE clustering analysis. The black filled square and circle are the x_{HI} estimates from the LAE LF evolution of Konno et al. (2017) and Konno et al. (2014), respectively. The open circles are the constraints at $z = 6.6$ obtained by Ouchi et al. (2010) from the evolution of Ly α LF (left circle) and clustering (right circle), while the open diamond and the open pentagon represent the upper limits from the Ly α LF evolution to $z = 6.5$ given by Malhotra & Rhoads (2004) and Kashikawa et al. (2006). Here, we add small offsets along redshift to the positions of the filled square, the open circles, and the open diamond, avoiding overlapping symbols. The filled hexagon and the filled pentagons show the constraints from a spectrum of a GRB (Gallerani et al. 2008b) and statistics of QSO dark-gaps (Gallerani et al. 2008a), respectively. The open hexagons are the constraints calculated from the Ly α damping wing absorption of GRBs at $z = 6.3$ (Totani et al. 2006) and $z = 5.9$ (Totani et al. 2016). The filled diamonds indicate the QSO Gunn-Peterson optical depth measurement results (Fan et al. 2006). The triangle denotes the 1σ lower-limit of redshift obtained by Planck 2015 (Planck Collaboration et al. 2016) in the case of instantaneous reionization. The solid line and the gray shade indicate the best-estimate and the uncertainty of the x_{HI} evolution (Ishigaki et al. 2017) that agrees the evolutions of τ_e and ρ_{UV} with free parameters including the ionizing photon escape fraction. The dotted, dashed, and dot-dashed lines are the evolution of x_{HI} for the reionizing sources down to the massive halos, the moderately massive halos, and the mini-halos, respectively, in the model of Choudhury et al. (2008). The dashed double-dotted line indicates the prediction of the double reionization model (Cen 2003).

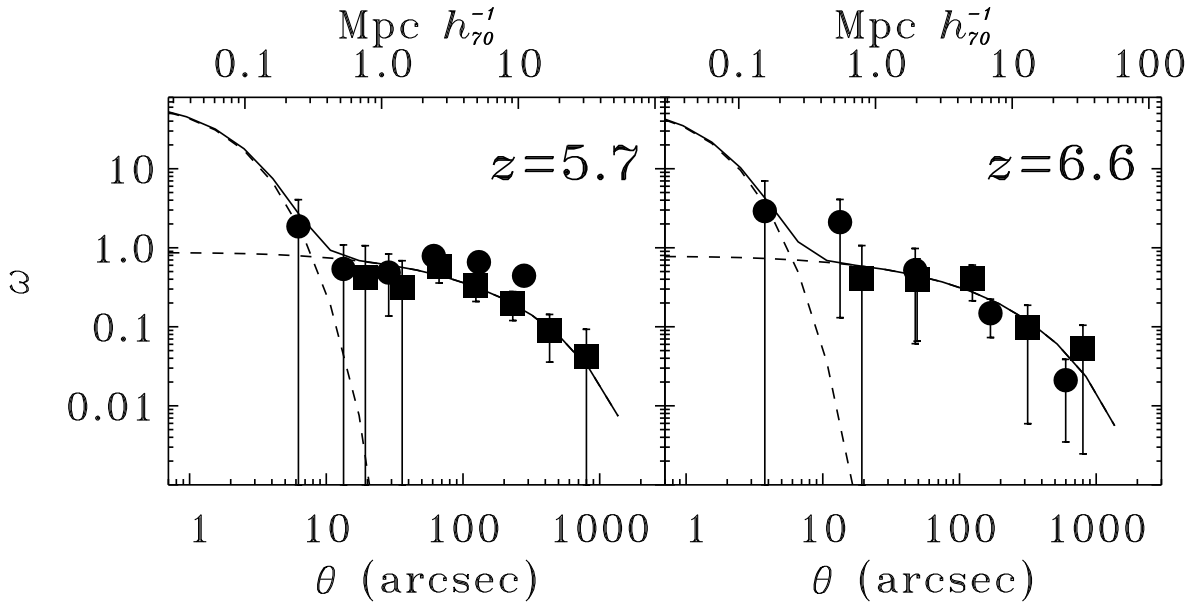


Fig. 10. Best-fit HOD models of the LAEs at $z = 5.7$ (left) and 6.6 (right). The solid lines represent the best-fit HOD models, while the dashed lines denote the breakdowns of the best-fit HOD models, 1 and 2 halo terms. The squares and circles are the ACF measurements that are the same as those in Figure 6.

et al. 2006; Totani et al. 2014; Totani et al. 2016; see also Greiner et al. 2009), and galaxies including LAEs (Malhotra & Rhoads 2004; Ouchi et al. 2010; Ota et al. 2010; Kashikawa et al. 2011; Pentericci et al. 2011; Ono et al. 2012; Treu et al. 2013; Caruana et al. 2014; Konno et al. 2014; Schenker et al. 2014; Konno et al. 2017). Our results agree with the previous LAE clustering results of Ouchi et al. (2010). Our constraint on x_{HI} is stronger than the one of Ouchi et al. (2010), due to the fact that the statistical uncertainties of the ACF measurements of this study are smaller than those of Ouchi et al. (2010). This is because the number of LAEs in this study is larger than the one of Ouchi et al. (2010). Moreover, our x_{HI} estimate agrees with many of the estimates and constraints obtained by the other independent objects (QSOs, GRBs, and galaxies) and methods (Gunn-Peterson and $\text{Ly}\alpha$ DW absorptions) in the previous studies. It should be noted that the results of GRBs have a large scatter. This scatter is probably made by the systematic uncertainty raised by the sightline variance effects. The numerical simulations of McQuinn et al. (2008) suggest that the patchiness of reionization gives the systematic error of $\delta x_{\text{HI}} \sim 0.3$ in an x_{HI} measurement of a single GRB sightline.

5.2 Hosting Dark-Matter Halo

Figure 9 presents evolution of x_{HI} determined by Ishigaki et al. (2017) who use all of the observational results related to reionization, CMB Thomson scattering optical depth τ_e , UV luminosity density ρ_{UV} , and the ionized fraction Q_{HII} obtained to date, based on the standard analytical model (Madau et al. 1999; Robertson et al. 2015) fitting that allows a wide param-

eter range of unknown parameters such as the ionizing-photon escape fraction. It should be noted that the Ishigaki et al.'s (2017) result of x_{HI} evolution agrees with the τ_e measurement of Planck2016. We find in Figure 9 that the evolution of x_{HI} (the solid curve) is consistent with our x_{HI} estimate from the LAE clustering, supportive of the moderately late reionization scenario suggested by Ishigaki et al. (2017).

5.2.1 Halo Occupation Distribution Modeling

We carry out halo occupation distribution (HOD) modeling for our ACFs that are the encodes of the hosting dark-matter halo properties. Note that the ACF of the LAEs at $z = 5.7$ is not affected by the effects of patchy ionized bubbles of cosmic reionization (Section 1), because $z = 5.7$ corresponds to the post-reionization epoch. However, the LAE ACF at $z = 6.6$ may be strengthened by the selective escapes of $\text{Ly}\alpha$ photons from patchy ionized bubbles probably existing at this redshift, although the $z = 6.6$ LAE ACF appears weakly to be affected by cosmic reionization (Section 5.1.1). In this section, we perform the HOD modeling for the ACF of the LAEs at $z = 5.7$ for the secure results. Moreover, we conduct the same analysis for the LAEs at $z = 6.6$ under the assumption that the reionization effect is negligibly small, following our results that the influence of cosmic reionization is not large at $z = 6.6$ (Section 5.1.1).

We adopt the HOD models of Harikane et al. (2016) based on the halo mass function of Behroozi et al. (2013) that is a modification of the Tinker et al. (2008) halo mass function. In the HOD models of Harikane et al. (2016), there are a total of five parameters, M_{min} , M_1' , α , M_0 , and $\sigma_{\log M}$. Here, M_{min}

Table 2. Properties of Dark-Matter Halos of the LAEs Estimated with the HOD Model

z	$L_{\text{Ly}\alpha}^{\text{th}}$ ($10^{42} \text{ erg s}^{-1}$)	$\log(M_{\text{min}}/M_{\odot})$	$\log(\langle M \rangle / M_{\odot})$	$b_{\text{g}}^{\text{HOD}}$	$f_{\text{duty}}^{\text{LAE}}$ (10^{-4})	χ^2/dof
(1)	(2)	(3)	(4)	(5)	(6)	(7)
5.7	6.3	$9.5^{+0.5}_{-1.2}$	$11.1^{+0.2}_{-0.4}$	$3.9^{+0.7}_{-1.0}$	$7.7^{+53.0}_{-7.6}$	1.1/6
6.6 [†]	7.9	$9.1^{+0.7}_{-1.9}$	$10.8^{+0.3}_{-0.5}$	$4.1^{+1.0}_{-1.4}$	$0.9^{+13.5}_{-0.9}$	1.1/4

[†] The results of $z = 6.6$ LAEs may be weakly affected by the reionization effects (see text).

is the mass of the dark-matter halo that hosts a galaxy at the possibility of 50%. The values of M'_1 and α are the normalization and the slope of the power law, respectively, for the satellite galaxy occupation number. We define M_0 and $\sigma_{\log M}$ as the halo mass cut off and the halo-mass transition width of the central and satellite galaxies, respectively. We do not include the parameter of the duty cycle in our HOD modeling, because the number density is not used in our fitting. Instead, we compare the number densities given by our HOD modeling and our observations to constrain the duty cycle of LAEs, which are detailed in Section 5.2.2. Following Harikane et al. (2016), we adopt the two relations, $\log M_0 = 0.76 \log M'_1 + 2.3$ and $\log M'_1 = 1.18 \log M_{\text{min}} - 1.28$. We assume $\sigma_{\log M} = 0.2$ and $\alpha = 1$ that are suggested by the fitting results of Zheng et al. (2007). although we confirm that the choice of these two parameters do not change our conclusions. We thus obtain the best-fit HOD models (i.e. M_{min} values) by χ^2 minimization. Figure 10 presents the best-fit HOD models, and Table 2 summarizes the best-fit M_{min} values. We define the average dark-matter halo mass $\langle M_{\text{h}} \rangle$ and the average galaxy bias $b_{\text{g}}^{\text{HOD}}$ from the HOD modeling results,

$$\langle M_{\text{h}} \rangle = \frac{\int_{M_{\text{h}}^{\text{min}}}^{\infty} M N_{\text{g}} n dM}{\int_{M_{\text{h}}^{\text{min}}}^{\infty} N_{\text{g}} n dM} \quad \text{and} \quad (10)$$

$$b_{\text{g}}^{\text{HOD}} = \frac{\int_{M_{\text{h}}^{\text{min}}}^{\infty} b N_{\text{g}} n dM}{\int_{M_{\text{h}}^{\text{min}}}^{\infty} N_{\text{g}} n dM}, \quad (11)$$

where n and b are the number density and the bias of dark-matter halos, respectively, with a dark-matter halo mass M_{h} (Behroozi et al. 2013; Tinker et al. 2010). The value of N_{g} is a galaxy occupation function at M_{h} that is determined by the HOD modeling. The values of $\langle M_{\text{h}} \rangle$ and $b_{\text{g}}^{\text{HOD}}$ for our LAEs are summarized in Table 2. We find that the average dark-matter halo masses of the $\gtrsim L^*$ LAEs are moderately small, $\log(\langle M_{\text{h}} \rangle / M_{\odot}) = 11.1^{+0.2}_{-0.4}$ at $z = 5.7$ and $\log(\langle M_{\text{h}} \rangle / M_{\odot}) = 10.8^{+0.3}_{-0.5}$ at $z = 6.6$ that are consistent with the previous estimates ($\log(\langle M_{\text{h}} \rangle / M_{\odot}) \sim 10 - 11$) by clustering analysis (Ouchi et al. 2010). The values of $b_{\text{g}}^{\text{HOD}}$ are consistent with those of b_{avg} (Table 1) within the errors.

5.2.2 Duty Cycle

It is suggested that LAEs do not exist in all of the dark-matter halos more massive than $M_{\text{h}}^{\text{min}}$ (e.g. Ouchi et al. 2010), because

LAEs should meet two physical conditions: i) LAEs should be active star-forming galaxies producing Ly α photons and ii) LAE's Ly α photons should largely escape from the ISM. In other words, not all of galaxies in a dark-matter halo can be LAEs. We evaluate the duty cycle of LAEs (i.e. $f_{\text{duty}}^{\text{LAE}}$) that is defined by the probability that a dark-matter halo beyond the minimum-halo mass hosts an LAE(s). With f_{duty} , one can calculate the galaxy number density,

$$n_{\text{g}} = \int_{M_{\text{h}}^{\text{min}}}^{\infty} f_{\text{duty}}^{\text{LAE}} N_{\text{g}} n dM. \quad (12)$$

We derive $f_{\text{duty}}^{\text{LAE}}$ with the best-fit HOD parameters, assuming that $f_{\text{duty}}^{\text{LAE}}$ does not depend on the dark-matter halo mass. The observational measurements of n_{g} are taken from the HSC SILVERRUSH paper of Konno et al. (2017). We thus obtain $f_{\text{duty}}^{\text{LAE}} = 7.7^{+53.0}_{-0.75} \times 10^{-4}$ and $0.9^{+13.5}_{-0.9} \times 10^{-4}$ for our LAEs at $z = 5.7$ and 6.6 , respectively, that are listed in Table 2. Although $f_{\text{duty}}^{\text{LAE}}$ is very poorly constrained with the large uncertainties, we find that the duty cycle of LAEs is $\sim 1\%$ or less at $z = 5.7$ and 6.6 . These small duty cycle values for $z = 6 - 7$ LAEs are consistent with the previous estimates by the similar technique (Ouchi et al. 2010). The small duty cycle values indicate that dark-matter halos hosting LAEs are rare, and that majority of LAEs are populated in abundant low-mass dark matter halos with a mass close to the minimum-halo mass.

5.2.3 Galaxy Formation and LAEs

Figure 7 presents the evolutionary tracks of dark-matter halos for the galaxy-conserving model and the constant-mass model. For the galaxy-conserving models, we assume that the gravity drives the motion of galaxies under the condition of no mergers. The bias evolution in the galaxy-conserving model (Fry 1996) is described as

$$b_{\text{g}} = 1 + (b_{\text{g}}^0 - 1)/D(z), \quad (13)$$

where $D(z)$ and b_{g}^0 are the growth factor and the bias at $z = 0$, respectively. If one assumes the galaxy-conserving evolution, our LAEs at $z = 5.7$ and 6.6 evolve into the present-galaxies with $b_{\text{g}}^0 \sim 1.6 - 1.7$. Galaxies with $b_{\text{g}}^0 \sim 1.6 - 1.7$ are massive bright $\sim 6L^*$ galaxies today (Zehavi et al. 2005). The galaxy-conserving evolution suggests that our LAEs at $z = 5.7$ and 6.6 are the progenitors of very massive bright galaxies in the present-day universe.

6 Summary

We investigate clustering of Ly α emitters (LAEs) at $z = 5.7$ and 6.6 with the early data of the Hyper Suprime-Cam (HSC) Subaru Strategic Program (first-data release shown in Aihara et al. 2017), and introduce the program of Systematic Identification of LAEs for Visible Exploration and Reionization Research Using Subaru HSC (SILVERRUSH). From the early data, we obtain the unprecedentedly large samples of $1,832 \gtrsim L^*$ LAEs at $z = 6 - 7$ over the total area of $14 - 21 \text{ deg}^2$ that is about an order of magnitude larger than the previous $z = 6 - 7$ LAE clustering studies. Based on the LAE clustering measurements, we study cosmic reionization and galaxy formation, comparing theoretical models. In this study, there are two major results that are summarized below.

1. We calculate angular correlation functions of the $z = 6 - 7$ LAEs. The correlation lengths are estimated to be $r_0 = 3.01^{+0.35}_{-0.35}$ and $2.66^{+0.49}_{-0.70} h_{100}^{-1} \text{ Mpc}$ for the $\gtrsim L^*$ LAEs at $z = 5.7$ and 6.6 , respectively. The average of the large-scale bias value is $b_{\text{avg}} = 4.13 \pm 0.17$ (4.54 ± 0.63) at $z = 5.7$ ($z = 6.6$) for the LAEs. Because Ly α photons emitted from LAEs in ionized bubbles can selectively escape from the partly neutral IGM at the EoR, observed LAEs at $z = 6.6$ should have clustering signals stronger than the intrinsic clustering. Based on this physical picture, we obtain the constraint of $x_{\text{HI}} = 0.15^{+0.15}_{-0.15}$ at $z = 6.6$ by the comparisons between our clustering measurements and two independent theoretical models.

2. We study the $\gtrsim L^*$ LAE clustering by the halo occupation distribution (HOD) modeling. (Here, for the LAE clustering at the EoR of $z = 6.6$, we assume that the LAE clustering is not largely impacted by the cosmic reionization.) The best-fit models indicate that the $\gtrsim L^*$ LAEs are hosted by the dark-matter halos with average masses of $\log(\langle M_h \rangle / M_\odot) = 11.1^{+0.2}_{-0.4}$ and $10.8^{+0.3}_{-0.5}$ at $z = 5.7$ and 6.6 , respectively. Comparing the number densities of observed LAEs and those suggested from the HOD modeling, we find that dark-matter halos of only 1 % (or less) down to the minimum-halo mass can host the $\gtrsim L^*$ LAEs. With the standard structure formation models, the bias evolution of the dark-matter halos indicates that the $\gtrsim L^*$ LAEs at $z = 6 - 7$ are progenitors of massive $\sim 6L^*$ galaxies in the present-day universe.

Acknowledgments

We are grateful to useful discussion with Mark Dijkstra, Richard Ellis, Andrea Ferrara, Martin Haehnelt, Alex Hagen, Koki Kakiichi, Andrei Mesinger, Naveen Reddy, and Zheng Zheng. We acknowledge Jirong Mao and Anne Hutter for their comments. The Hyper Suprime-Cam (HSC) collaboration includes the astronomical communities of Japan and Taiwan, and Princeton University. The HSC instrumentation and software were developed by the National Astronomical Observatory of Japan (NAOJ), the Kavli Institute for the Physics and Mathematics of the Universe (Kavli IPMU), the University of Tokyo, the

High Energy Accelerator Research Organization (KEK), the Academia Sinica Institute for Astronomy and Astrophysics in Taiwan (ASIAA), and Princeton University. Funding was contributed by the FIRST program from Japanese Cabinet Office, the Ministry of Education, Culture, Sports, Science and Technology (MEXT), the Japan Society for the Promotion of Science (JSPS), Japan Science and Technology Agency (JST), the Toray Science Foundation, NAOJ, Kavli IPMU, KEK, ASIAA, and Princeton University. The NB816 filter was supported by Ehime University (PI: Y. Taniguchi). The NB921 filter was supported by KAKENHI (23244025) Grant-in-Aid for Scientific Research (A) through the Japan Society for the Promotion of Science (PI: M. Ouchi). This paper makes use of software developed for the Large Synoptic Survey Telescope. We thank the LSST Project for making their code available as free software at <http://dm.lsst.org>. The Pan-STARRS1 Surveys (PS1) have been made possible through contributions of the Institute for Astronomy, the University of Hawaii, the Pan-STARRS Project Office, the Max-Planck Society and its participating institutes, the Max Planck Institute for Astronomy, Heidelberg and the Max Planck Institute for Extraterrestrial Physics, Garching, The Johns Hopkins University, Durham University, the University of Edinburgh, Queens University Belfast, the Harvard-Smithsonian Center for Astrophysics, the Las Cumbres Observatory Global Telescope Network Incorporated, the National Central University of Taiwan, the Space Telescope Science Institute, the National Aeronautics and Space Administration under Grant No. NNX08AR22G issued through the Planetary Science Division of the NASA Science Mission Directorate, the National Science Foundation under Grant No. AST-1238877, the University of Maryland, and Eotvos Lorand University (ELTE) and the Los Alamos National Laboratory. This work is supported by World Premier International Research Center Initiative (WPI Initiative), MEXT, Japan, and KAKENHI (15H02064) Grant-in-Aid for Scientific Research (A) through Japan Society for the Promotion of Science. Based on data collected at the Subaru Telescope and retrieved from the HSC data archive system, which is operated by Subaru Telescope and Astronomy Data Center at National Astronomical Observatory of Japan.

References

- Aihara, H., Armstrong, R., Bickerton, S., et al. 2017, arXiv:1702.08449
- Ando, M., Ohta, K., Iwata, I., Akiyama, M., Aoki, K., & Tamura, N. 2006, *ApJL*, 645, L9
- Bacon, R., Accardo, M., Adjali, L., et al. 2010, *Proc. SPIE*, 7735, 773508
- Behroozi, P. S., Wechsler, R. H., & Conroy, C. 2013, *ApJ*, 770, 57
- Bolton, J. S., Haehnelt, M. G., Warren, S. J., et al. 2011, *MNRAS*, 416, L70
- Bosch, J., Armstrong, R., Bickerton, S., et al. 2017, arXiv:1705.06766
- Caruana, J., Bunker, A. J., Wilkins, S. M., et al. 2014, *MNRAS*, 443, 2831
- Cen, R. 2003, *ApJ*, 591, 12
- Choudhury, T. R., Ferrara, A., & Gallerani, S. 2008, *MNRAS*, 385, L58
- Cowie, L. L., & Hu, E. M. 1998, *AJ*, 115, 1319
- Cowie, L. L., Barger, A. J., & Hu, E. M. 2010, *ApJ*, 711, 928
- Deharveng, J.-M., Small, T., Barlow, T. A., et al. 2008, *ApJ*, 680, 1072-1082
- Efstathiou, G., Bernstein, G., Tyson, J. A., Katz, N., & Guhathakurta, P. 1991, *ApJL*, 380, L47
- Fan, X., et al. 2006, *AJ*, 132, 117
- Finkelstein, S. L., Cohen, S. H., Moustakas, J., et al. 2011, *ApJ*, 733, 117
- Finkelstein, S. L., Papovich, C., Dickinson, M., et al. 2013, *Nature*, 502, 524

- Fry, J. N. 1996, *ApJL*, 461, L65
- Furlanetto, S. R., Zaldarriaga, M., & Hernquist, L. 2006, *MNRAS*, 365, 1012
- Gallerani, S., Ferrara, A., Fan, X., & Choudhury, T. R. 2008, *MNRAS*, 386, 359
- Gallerani, S., Salvaterra, R., Ferrara, A., & Choudhury, T. R. 2008, *MNRAS*, 388, L84
- Gawiser, E., et al. 2007, *ApJ*, 671, 278
- Greiner, J., et al. 2009, *ApJ*, 693, 1610
- Groth, E. J. & Peebles, P. J. E. 1977, *ApJ*, 217, 385
- Guaia, L., et al. 2010, *ApJ*, 714, 255
- Guaia, L., Francke, H., Gawiser, E., et al. 2013, *A&A*, 551, A93
- Hagen, A., Ciardullo, R., Gronwall, C., et al. 2014, *ApJ*, 786, 59
- Harikane, Y., Ouchi, M., Ono, Y., et al. 2016, *ApJ*, 821, 123
- Harikane, Y., Ouchi, M., Ono, Y., et al. 2017, *arXiv:1704.06535*
- Hashimoto, T., Verhamme, A., Ouchi, M., et al. 2015, *ApJ*, 812, 157
- Hayashino, T., Matsuda, Y., Tamura, H., et al. 2004, *AJ*, 128, 2073
- Hill, G. J., Tuttle, S. E., Lee, H., et al. 2012, *Proc. SPIE*, 8446, 84460N
- Hu, E. M., & McMahon, R. G. 1996, *Nature*, 382, 231
- Hu, E. M., Cowie, L. L., Barger, A. J., et al. 2010, *ApJ*, 725, 394
- Hutter, A., Dayal, P., & Müller, V. 2015, *MNRAS*, 450, 4025
- Ichikawa, T., et al. 2007, *PASJ*, 59, 1081
- Iliev, I. T., Shapiro, P. R., McDonald, P., Mellema, G., & Pen, U.-L. 2008, *MNRAS*, 391, 63
- Inoue, A. et al., to be submitted to *PASJ*
- Ishigaki, M., Kawamata, R., Ouchi, M., Oguri, M., & Shimasaku, K. 2017, *arXiv:1702.04867*
- Kakiichi, K., Dijkstra, M., Ciardi, B., & Graziani, L. 2016, *MNRAS*, 463, 4019
- Kashikawa, N., et al. 2006, *ApJ*, 648, 7
- Kashikawa, N., Shimasaku, K., Matsuda, Y., et al. 2011, *ApJ*, 734, 119
- Kobayashi, M. A. R., Totani, T., & Nagashima, M. 2010, *ApJ*, 708, 1119
- Kojima, T., Ouchi, M., Nakajima, K., et al. 2016, *arXiv:1605.03436*
- Konno, A., Ouchi, M., Ono, Y., et al. 2014, *ApJ*, 797, 16
- Konno, A., Ouchi, M., Nakajima, K., et al. 2016, *ApJ*, 823, 20
- Konno, A., Ouchi, M., Shibuya, T., et al. 2017, *arXiv:1705.01222*
- Kovač, K., Somerville, R. S., Rhoads, J. E., Malhotra, S., & Wang, J. 2007, *ApJ*, 668, 15
- Lacey, C., & Cole, S. 1993, *MNRAS*, 262, 627
- Landy, S. D. & Szalay, A. S. 1993, *ApJ*, 412, 64
- Larson, D., Dunkley, J., Hinshaw, G., et al. 2011, *ApJS*, 192, 16
- Le Delliou, M., Lacey, C. G., Baugh, C. M., & Morris, S. L. 2006, *MNRAS*, 365, 712
- Lee, K.-S., Giavalisco, M., Gnedin, O. Y., Somerville, R. S., Ferguson, H. C., Dickinson, M., & Ouchi, M. 2006, *ApJ*, 642, 63
- Lidz, A., Zahn, O., Furlanetto, S. R., McQuinn, M., Hernquist, L., & Zaldarriaga, M. 2009, *ApJ*, 690, 252
- Ling, E. N., Barrow, J. D., & Frenk, C. S. 1986, *MNRAS*, 223, 21P
- Madau, P., Haardt, F., & Rees, M. J. 1999, *ApJ*, 514, 648
- Malhotra, S., & Rhoads, J. E. 2004, *ApJL*, 617, L5
- Mao, J., Lapi, A., Granato, G. L., de Zotti, G., & Danese, L. 2007, *ApJ*, 667, 655
- Matsuda, Y., Yamada, T., Hayashino, T., et al. 2004, *AJ*, 128, 569
- Matthee, J., Sobral, D., Santos, S., et al. 2015, *MNRAS*, 451, 400
- McLure, R. J., Cirasuolo, M., Dunlop, J. S., Foucaud, S., & Almaini, O. 2009, *MNRAS*, 395, 2196
- McQuinn, M., Hernquist, L., Zaldarriaga, M., & Dutta, S. 2007, *MNRAS*, 381, 75
- McQuinn, M., Lidz, A., Zaldarriaga, M., Hernquist, L., & Dutta, S. 2008, *MNRAS*, 388, 1101
- Miyazaki, S. et al. in preparation
- Momose, R., Ouchi, M., Nakajima, K., et al. 2014, *MNRAS*, 442, 110
- Momose, R., Ouchi, M., Nakajima, K., et al. 2016, *MNRAS*, 457, 2318
- Mortlock, D. J., Warren, S. J., Venemans, B. P., et al. 2011, *Nature*, 474, 616
- Murayama, T., et al. 2007, *ApJS*, 172, 523
- Nagamine, K., Ouchi, M., Springel, V., & Hernquist, L. 2010, *PASJ*, 62, 1455
- Nakajima, K., Ouchi, M., Shimasaku, K., et al. 2012, *ApJ*, 745, 12
- Nakajima, K., & Ouchi, M. 2014, *MNRAS*, 442, 900
- Oesch, P. A., van Dokkum, P. G., Illingworth, G. D., et al. 2015, *ApJL*, 804, L30
- Ono, Y., Ouchi, M., Mobasher, B., et al. 2012, *ApJ*, 744, 83
- Ono, Y., Ouchi, M., Harikane, Y., et al. 2017, *arXiv:1704.06004*
- Ota, K., Iye, M., Kashikawa, N., et al. 2010, *ApJ*, 722, 803
- Ota, K., Iye, M., Kashikawa, N., et al. 2017, *arXiv:1703.02501*
- Ouchi, M., et al. 2003, *ApJ*, 582, 60
- Ouchi, M., et al. 2005, *ApJL*, 620, L1
- Ouchi, M., et al. 2005, *ApJL*, 635, L117
- Ouchi, M., et al. 2008, *ApJS*, 176, 301
- Ouchi, M., et al. 2009a, *ApJ*, 696, 1164
- Ouchi, M., Shimasaku, K., Furusawa, H., et al. 2010, *ApJ*, 723, 869
- Ouchi, M., Ellis, R., Ono, Y., et al. 2013, *ApJ*, 778, 102
- Partridge, R. B., & Peebles, P. J. E. 1967, *ApJ*, 147, 868
- Pascarella, S. M., Windhorst, R. A., Keel, W. C., & Odewahn, S. C. 1996, *Nature*, 383, 45
- Peacock, J. A., & Dodds, S. J. 1994, *MNRAS*, 267, 1020
- Peebles, P. J. E. 1980, *The Large-Scale Structure of the Universe* (Princeton: Princeton Univ. Press)
- Pentericci, L., Fontana, A., Vanzella, E., et al. 2011, *ApJ*, 743, 132
- Planck Collaboration, Ade, P. A. R., Aghanim, N., et al. 2016, *A&A*, 594, A13
- Rhoads, J. E., Malhotra, S., Dey, A., et al. 2000, *ApJL*, 545, L85
- Robertson, B. E., Ellis, R. S., Furlanetto, S. R., & Dunlop, J. S. 2015, *ApJL*, 802, L19
- Saito, T., Shimasaku, K., Okamura, S., et al. 2006, *ApJ*, 648, 54
- Salvadori, S., Dayal, P., & Ferrara, A. 2010, *arXiv:1005.4422*
- Schenker, M. A., Ellis, R. S., Konidaris, N. P., & Stark, D. P. 2014, *ApJ*, 795, 20
- Sheth, R. K. & Tormen, G. 1999, *MNRAS*, 308, 119
- Shibuya, T., Kashikawa, N., Ota, K., et al. 2012, *ApJ*, 752, 114
- Shibuya, T., Ouchi, M., Nakajima, K., et al. 2014, *ApJ*, 788, 74
- Shibuya, T., Ouchi, M., Konno, A., et al. 2017a, *arXiv:1704.08140*
- Shibuya, T., Ouchi, M., Harikane, Y., et al. 2017b, *arXiv:1705.00733*
- Shimasaku, K., et al. 2003, *ApJL*, 586, L111
- Simon, P. 2007, *A&A*, 473, 711
- Sobral, D., Matthee, J., Darvish, B., et al. 2015, *ApJ*, 808, 139
- Santos, S., Sobral, D., & Matthee, J. 2016, *MNRAS*, 463, 1678
- Sobacchi, E., & Mesinger, A. 2015, *MNRAS*, 453, 1843
- Stark, D. P., Walth, G., Charlot, S., et al. 2015, *MNRAS*, 454, 1393
- Steidel, C. C., Adelberger, K. L., Shapley, A. E., et al. 2000, *ApJ*, 532, 170
- Steidel, C. C., Bogosavljević, M., Shapley, A. E., et al. 2011, *ApJ*, 736, 160
- Tinker, J., Kravtsov, A. V., Klypin, A., et al. 2008, *ApJ*, 688, 709-728
- Tinker, J. L., Robertson, B. E., Kravtsov, A. V., et al. 2010, *ApJ*, 724, 878

- Toshikawa, J., et al. 2017 submitted to PASJ
- Totani, T., Kawai, N., Kosugi, G., Aoki, K., Yamada, T., Iye, M., Ohta, K., & Hattori, T. 2006, PASJ, 58, 485
- Totani, T., Aoki, K., Hattori, T., et al. 2014, PASJ, 66, 63
- Totani, T., Aoki, K., Hattori, T., & Kawai, N. 2016, PASJ, 68, 15
- Treu, T., Schmidt, K. B., Trenti, M., Bradley, L. D., & Stiavelli, M. 2013, ApJL, 775, L29
- Verhamme, A., Schaerer, D., Atek, H., & Tapken, C. 2008, A&A, 491, 89
- Zehavi, I., Zheng, Z., Weinberg, D. H., et al. 2005, ApJ, 630, 1
- Zheng, Z., Coil, A. L., & Zehavi, I. 2007, ApJ, 667, 760
- Zheng, Z., Cen, R., Weinberg, D., Trac, H., & Miralda-Escudé, J. 2011, ApJ, 739, 62
- Zheng, Z.-Y., Wang, J., Rhoads, J., et al. 2017, arXiv:1703.02985
- Zitrin, A., Labbé, I., Belli, S., et al. 2015, ApJL, 810, L12